Li *et al. Energy Mater* 2024;4:400009
**DOI:** 10.20517/energymater.2023.78

**Energy Materials**

**Article**

**Open Access**

Check for updates

# Binary anion and cation co-doping enhance sulfide solid electrolyte performance for all-solid-state lithium batteries

**Cheng Li[1], Yuqi Wu[1], Zhongwei Lv[1], Jinxue Peng[1], Jun Liu[1], Xuefan Zheng[1], Yongmin Wu[2], Weiping Tang[2], Zhengliang Gong[1,*], Yong Yang[1,3,*]**

[1]College of Energy, Xiamen University, Xiamen 361102, Fujian, China.
[2]State Key Laboratory of Space Power-Sources Technology, Shanghai Institute of Space Power-Sources, Shanghai 200245, China.
[3]College of Chemistry and Chemical Engineering & Tan Kah Kee Innovation Laboratory (IKKEM), Xiamen University, Xiamen 361102, Fujian, China.

***Correspondence to:** Prof. Zhengliang Gong, College of Energy, Xiamen University, Xiamen 361102, Fujian, China. E-mail: zlgong@xmu.edu.cn; Prof. Yong Yang, State Key Laboratory of Physical Chemistry of Solid Surfaces, Department of Chemistry and College of Chemistry and Chemical Engineering & Tan Kah Kee Innovation Laboratory (IKKEM), Xiamen University, Xiamen 361102, Fujian, China. E-mail: yyang@xmu.edu.cn

**How to cite this article:** Li C, Wu Y, Lv Z, Peng J, Liu J, Zheng X, Wu Y, Tang W, Gong Z, Yang Y. Binary anion and cation co-doping enhance sulfide solid electrolyte performance for all-solid-state lithium batteries. *Energy Mater* 2024;4:400009. https://dx.doi.org/10.20517/energymater.2023.78

**Received:** 30 Sep 2023 **First Decision:** 10 Nov 2023 **Revised:** 30 Nov 2023 **Accepted:** 13 Dec 2023 **Published:** 11 Jan 2024

**Academic Editors:** Jiazhao Wang, Nicolas Alonso-Vante **Copy Editor:** Fangling Lan **Production Editor:** Fangling Lan

## Abstract

Sulfide solid electrolytes are regarded as a pivotal component for all-solid-state lithium batteries (ASSLBs) due to their inherent advantages, such as high ionic conductivity and favorable mechanical properties. However, persistent challenges related to electrochemical stability and interfacial compatibility have remained significant hurdles in their practical application. To address these issues, we propose an anion-cation co-doping strategy for the optimization of $Li_7P_3S_{11}$ (LPS) through chemical bonding and structural modifications. The co doping effects on the structural and electrochemical properties of $SiO_2$-, $GeO_2$-, and $SnO_2$-doped sulfide electrolytes were systematically investigated. Cations are found to preferentially substitute the $P^{5+}$ of the $P_2S_7^{4-}$ unit within the LPS matrix, thereby expanding the $Li^+$ diffusion pathways and introducing lithium defects to facilitate ion conduction. Concurrently, oxygen ions partially substitute sulfur ions, leading to improved electrochemical stability and enhanced interfacial performance of the sulfide electrolyte. The synergistic effects resulting from the incorporation of oxides yield several advantages, including superior ionic conductivity, enhanced interfacial stability, and effective suppression of lithium dendrite formation. Consequently, the application of oxide-doped sulfide solid electrolytes in

ASSLBs yields promising electrochemical performances. The cells with doped-electrolytes exhibit higher initial coulombic efficiency, superior rate capability, and cycling stability when compared to the pristine LPS. Overall, this research highlights the potential of oxide-doped sulfide solid electrolytes in the development of advanced ASSLBs.

**Keywords:** All-solid-state batteries, sulfide solid electrolyte, binary co-doping, $Li^+$ conductivity, electrochemical stability

## INTRODUCTION

With the burgeoning expansion in electronic devices, electric vehicles, and energy storage solutions, the demands placed on lithium-ion batteries have grown significantly[1-5]. Traditional lithium-ion batteries utilizing liquid electrolytes face safety concerns, and their energy density is approaching a plateau. By transitioning to solid electrolytes, all-solid-state lithium batteries (ASSLBs) have emerged as a promising solution to address these challenges. It shows great potential for these batteries to offer increased safety, durability, higher energy density, and greater flexibility in battery packaging design[6-10].

Solid electrolytes, a critical component of ASSLBs, have garnered increasing attention. Among various solid electrolytes, sulfide solid electrolytes have gained prominence due to their exceptional characteristics, including high ionic conductivity (> 1 mS $cm^{-1}$), favorable mechanical properties, and minimal grain boundary resistance. Nonetheless, solid-state batteries relying on sulfide electrolytes face significant hurdles, including poor air stability, chemical/electrochemical stability, and issues related to interfacial compatibility[11-15].

One of the most effective strategies for enhancing the stability of sulfide electrolytes is through element doping. Anion doping strategies have witnessed prominence, with partial substitution of sulfur by oxygen being the prevailing approach[16,17]. This strategy is widely employed because it confers notable benefits. Firstly, by incorporating oxygen atoms, the system forms non-bridging oxygen (O), which is more stable than bridging sulfur (S), thereby improving the overall stability of the electrolyte. Furthermore, the lattice mismatch between oxygen ions and oxide-based positive electrodes is minimal. Partially replacing sulfur with oxygen can effectively prevent oxygen from the positive electrode from infiltrating the sulfide electrolyte, thereby significantly inhibiting undesirable interface side reactions in sulfide-based ASSLBs. However, the incorporation of oxygen impedes the migration of $Li^+$. Notably, as the level of oxygen doping increases, the conductivity of the electrolyte may experience a gradual decline. On the other hand, when considering cation doping, the selection of dopants aligns with the Hard and Soft Acid-Base Theory (HSAB). According to this theory, hard acids have a preference for reacting with hard bases, while soft acids tend to react more readily with soft bases. Combining a softer acid, such as $Sn^{4+}$, $Ge^{4+}$, $As^{5+}$, and $Sb^{5+}$, with the soft base sulfur (S) can significantly enhance the air stability of the sulfide electrolyte[18-20].

Oxide doping constitutes a synergistic amalgamation of anion and cation doping methodologies, demonstrating the capability to concurrently enhance the conductivity and stability of sulfide electrolytes[21-25]. Liu *et al.* presented a pioneering endeavor by doping of $Li_3PS_4$ glass-ceramic electrolytes with ZnO, demonstrating the synthesis of a new $Li_{3+3x}P_{1-x}Zn_xS_{4-x}O_x$ solid electrolyte[26]. This advancement featured the incorporation of Zn, replacing a fraction of P, while O replaced a segment of S within the $Li_3PS_4$ matrix. The resultant electrolyte showcased enhanced air stability alongside improved ionic conductivity. Notably, there was no obvious structure change in the $Li_{3+3x}P_{1-x}Zn_xS_{4-x}O_x$ electrolyte after exposure to air. Ahmad *et al.* synthesized a $Li_{6.988}P_{2.994}Nb_{0.2}S_{10.934}O_{0.6}$ glass-ceramic electrolyte with Nb and O co-doping[27]. Wherein oxygen partially supplanted the sulfur bridge bond within the $P_2S_7^{4-}$ group, thereby engendering

the formation of $P_2OS_6^{4-}$ entities, which contributed significantly to augmenting the air stability of sulfide electrolyte. In addition, the increase in the crystallinity of the conductive phase coordinated a reduction in the activation energy associated with the migration of lithium ions, which culminated in an appreciable enhancement of ionic conductivity within the glass-ceramic electrolyte. Xu *et al.* introduced a congener substitution strategy to optimize the electrochemical performance of $Li_7P3S_{11}$ (LPS) via chemical bond and structural regulation[28]. The as-obtained $Li_7P_{2.9}Sb_{0.1}S_{10.75}O_{0.25}$ solid electrolyte shows improved solid-solid interfacial compatibility compared to LPS. Such enhancements are conducive to augmenting the reversible capacity, rate capability, coulombic efficiency, and cycling stability of ASSLBs. The oxide doping strategy has emerged as an effective methodology for mitigating the air sensitivity and instability issues associated with sulfide electrolytes without compromising the critical ionic conductivity. A systematic investigation of the effects of doping on the ionic conductivity, electrochemical stability, and interfacial stability is essential to guide the selection of appropriate doping elements and concentrations for optimizing the performance of the solid electrolytes.

In this work, the concurrent anion and cation co-doping strategy is proposed for optimizing the structural and electrochemical properties of LPS-based solid electrolytes employing oxides as deponents [Figure 1A]. We systematically investigate the effects of $SiO_2$, $GeO_2$, and $SnO_2$ doping on the structure, ionic conductivity, oxidative stability, and lithium plating/stripping behavior of $Li_{7+x}P_{3-x}M_xS_{11-2x}O_{2x}$ (M = Si, Ge, Sn) (LPS-$x$$MO_2$) electrolytes. The electrochemical performance of the doped LPS-$x$$MO_2$ electrolytes is evaluated in ASSLBs. It reveals that this co-doping strategy yields improved ionic conductivity and enhanced electrochemical stability. Specifically, $SnO_2$-doped LPS-$x$$SnO_2$ electrolytes exhibit higher ionic conductivity, while $SiO_2$-doped LPS-$x$$SiO_2$ electrolytes exhibit superior oxidative stability. Consequently, ASSLBs based on NCM811 cathodes and LPS-0.05$SnO_2$ electrolytes demonstrate higher initial capacity, while those utilizing LPS-0.05$SiO_2$ electrolytes exhibit superior initial coulombic efficiency, rate capability, and cycling stability.

## EXPERIMENTAL

### Preparation of solid-state electrolytes

$Li_{7+x}P_{3-x}M_xS_{11-2x}O_{2x}$ (M = Si, Ge, Sn, $x$ = 0, 0.02, 0.05, 0.08, 0.1) were synthesized through the high-energy ball-milling method combing with heat treatment techniques. $Li_2S$ (99.9%, Alfa Aesar), $P_2S_5$ (99%, $P \geq 27\%$, Macklin), and $SiO_2$, $GeO_2$, $SnO_2$ (99.995%, Aladdin) were used as raw materials, which were weighed based on the stoichiometric ratio in an Ar filled glove box. The weighed raw materials and the zirconia balls (10 mm in diameter) were subjected to a zirconia ceramic vial and ball-milled (PULVERISETTE 7, Fritsch, Germany) at 400 rpm for 10 h. The weight ratio of zirconia balls to materials was 20:1. The as-obtained precursors were sealed in a quartz tube and annealed at 210 °C for 3 h and 250 °C for 1 h with a heating rate of 1 °C $min^{-1}$. All the above processes were performed under Ar atmosphere.

### Material characterizations

X-ray diffraction (XRD) was used to analyze the crystalline phase of the sulfide solid-state electrolytes (SSE) by using a Rigaku Ultima IV X-ray Diffractometer (Rigaku Corporation, Japan) equipped with Cu K$\alpha$ radiation. Raman measurements were performed with a confocal Raman microscope (WITec Alpha, Ulm, Germany) with a 532 nm laser. Scanning electron microscopy (SEM) and energy dispersive X-ray spectroscopy (EDS) measurements were conducted using a SEM (ZIESS SUPRA 55, Germany). X-ray photoelectron spectroscopy (XPS) analysis was performed on a K-Alpha X-ray photoelectron spectrometer system (Thermo Scientific).

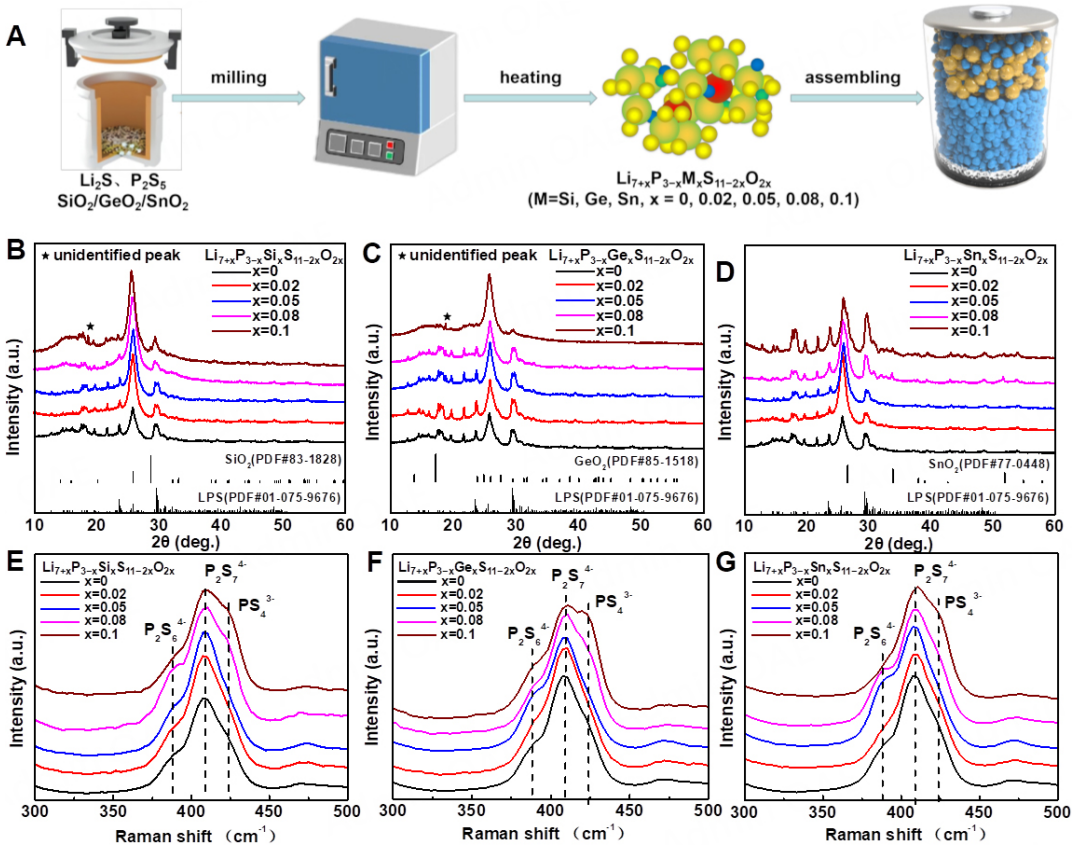


**Figure 1.** (A) Schematic illustrating the preparation process of sulfide electrolyte. X-ray diffraction patterns of the doped sulfide electrolytes (B) LPS-$x$SiO$_2$, (C) LPS-$x$GeO$_2$, (D) LPS-$x$SnO$_2$ ($x$ = 0, 0.02, 0.05, 0.08, 0.1) and Raman spectra of the doped sulfide electrolytes (E) LPS-$x$SiO$_2$, (F) LPS-$x$GeO$_2$, (G) LPS-$x$SnO$_2$ ($x$ = 0, 0.02, 0.05, 0.08, 0.1).

## Assembly of ASSLBs

$Li_{7.05}P_{2.95}M_{0.05}S_{10.9}O_{0.1}$ (M = Si, Ge, Sn) and LPS powders were used as solid electrolytes; single crystal NCM811 was used as the cathode material, and the Li/In alloy was used as the anode. The composite cathode was prepared by mixing NCM811, acetylene black (AB), and sulfide solid electrolytes with a weight ratio of 70:1:29. For the assembly of the ASSLBs, first, 100 mg of pristine LPS electrolyte powders were introduced into a PEEK tube (internal diameter of 10 mm) and subjected to cold-pressing at a pressure of 360 MPa. Subsequently, 10.0 mg of composite cathode material was uniformly distributed atop the electrolyte and cold-pressed under 360 MPa for three minutes. Then, the Li/In alloy (Li/In = 3:7) was positioned on the other side of the electrolyte, applying a pressure of 100 MPa for three minutes. All the battery assembly steps were conducted within an argon-filled glove box.

## Electrochemical measurements

The ionic conductivities of the sulfide solid electrolytes were measured by electrochemical impedance spectroscopy (EIS) using an Autolab PGSTA302 electrochemical workstation (Eco Chemie, Netherland) in a frequency range from 1 MHz to 0.1 Hz. Cyclic voltammetry (CV) was applied to evaluate the oxidative stability of the sulfide solid electrolytes, which was carried out with the sulfide solid-state batteries with composite material of LPS-$x$MO$_2$ and AB (LPS-$x$MO$_2$:AB = 6:4) as cathodes and lithium foil as anodes. The CV tests were carried out within the voltage range spanning from 2 to 4.5 V (*vs.* $Li^+$/Li), employing a scan rate of 0.1 mV $s^{-1}$. Li/LPS-$x$MO$_2$/Li symmetric cells were used to assess the electrochemical stability of the LPS-$x$MO$_2$ electrolytes against lithium metal anodes. The critical current density of the symmetric cells was

assessed at 30 °C with the applied current density incrementally increasing in steps of 0.06 mA $cm^{-2}$, and each Li plating/stripping step lasting 0.5 h. Galvanostatic charge-discharge tests were carried out using a battery test system (LAND CT2001A, Wuhan LAND Electronics. Ltd.) at room temperature within the voltage range of 2-3.7 V (*vs.* Li-In).

## RESULTS AND DISCUSSION

The crystal structure and structural units of the electrolytes were characterized through XRD and Raman spectroscopy. The XRD results [Figure 1B-D] show that when the doping amount is ≤ 0.05 mol, the diffraction patterns of the doped sample remain in congruence with that of the pristine LPS electrolyte, thus preserving an intact body-centered cubic structure. However, for doping concentration exceeding 0.08 mol, unidentified new diffraction peaks are evident, signifying the limits of dopant concentration. In addition, the lattice constant variation of LPS with an increasing concentration of $MO_2$ [Supplementary Table 1] and XRD patterns for reference materials (LPS, $MO_2$) [Supplementary Figure 1] was analyzed. It shows that as the doping concentration of $MO_2$ increases, the lattice parameters exhibit a gradual increase within the range of $0 \leq x \leq 0.08$, indicative of the successful incorporation of $MO_2$ into LPS. Raman spectra [Figure 1E-G] show peaks at approximately 407, 421 and 386 $cm^{-1}$ across all spectra. The peaks centered at 407 and 421 $cm^{-1}$ correspond to the symmetric stretching vibration of the P-S bonds in the $P_2S_7^{4-}$ and $PS_4^{3-}$ units, respectively, indicating the formation of a highly conductive crystalline LPS phase. A minor peak at approximately 386 $cm^{-1}$ corresponds to the low-conductivity phase of $Li_4P_2S_6$[29-31]. Furthermore, it is noteworthy that the moderate co-doping of anion and cation atoms into LPS exerts a relatively modest impact on the fundamental framework of the LPS-$x$$MO_2$ glass-ceramic electrolytes in comparison to the unaltered LPS electrolyte. Supplementary Figure 2 shows the morphology and element distribution of the typical LPS-0.05$MO_2$ (M = Si, Ge, Sn) electrolytes characterized by SEM. A typical spherical powder morphology is discernible, with diameters of about 1-3 μm. Notably, Si, Ge, Sn, and O elements are evenly distributed in the electrolyte particles.

The optimal doping concentration was determined by measuring the ionic conductivity of LPS-$x$$MO_2$ (M = Si, Ge, Sn, $x$=0, 0.02, 0.05, 0.08, 0.1) electrolytes through EIS employing a symmetrical SS/SSE/SS cell configuration [Figure 2A-C]. The ionic conductivity of pristine LPS was determined to be $1.07 \times 10^{-3}$ S $cm^{-1}$ [Supplementary Figure 3]. As the doping level increased, the ionic conductivities exhibited a gradual increment followed by a decline. Remarkably, LPS-0.05$SiO_2$, LPS-0.08$GeO_2$, and LPS-0.05$SnO_2$ electrolytes reached a peak ionic conductivity of $1.32 \times 10^{-3}$, $2.06 \times 10^{-3}$, and $2.53 \times 10^{-3}$ S $cm^{-1}$, respectively [Supplementary Figure 4]. The LPS-0.05$SnO_2$ electrolyte exhibits a 2.5 times improvement in ionic conductivity compared to pristine LPS. However, with further increasing doping levels, the EIS curves displayed a distinctive semicircle in the high-frequency region due to the presence of impurities in the electrolytes, consistent with XRD results [Supplementary Figure 5]. Moreover, the activation energies of the electrolytes were derived from Arrhenius plots based on the Arrhenius equation:

$$\sigma = A \exp(-Ea/KT)$$

where σ, T, $k$, and A represent the $Li^+$ conductivity, the absolute temperature, the Boltzmann constant, and the pre-exponential factor, respectively. The Arrhenius plots of activation energy are presented in Figure 2D-F. Notably, at higher doping concentrations, the electrolytes exhibited elevated activation energies, indicative of more pronounced barriers to lithium-ion migration.

It was found that the ionic conductivity of glass-ceramic electrolytes is correlated to the proportion of the high conductive crystalline LPS phase characterized by the typical local structural units of $P_2S_7^{4-}$ and $PS_4^{3-}$[32].

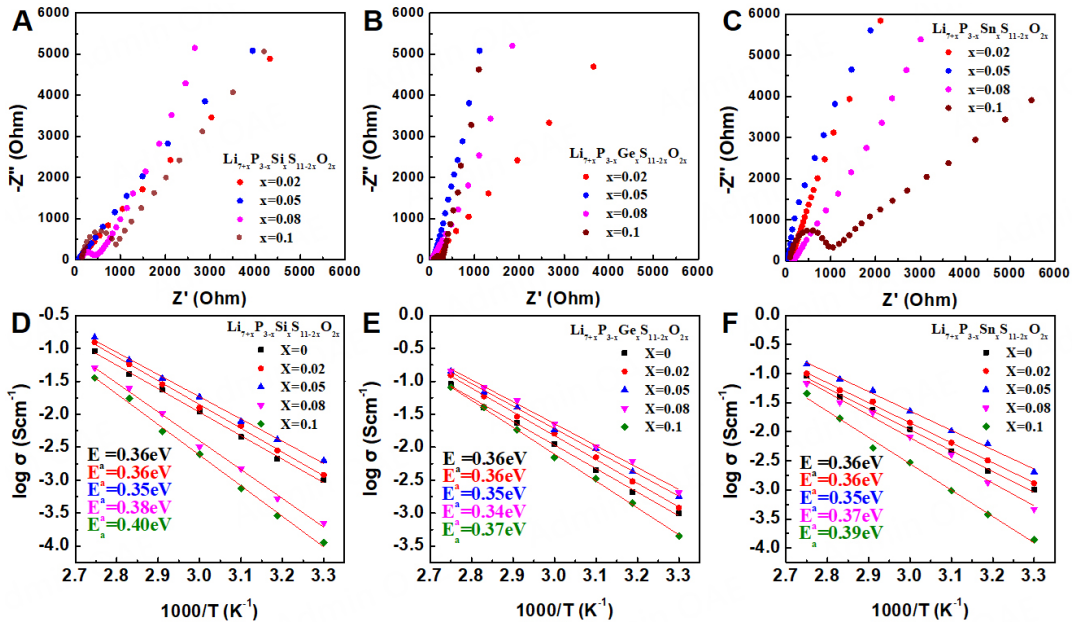


**Figure 2.** Nyquist plots for the solid electrolytes measured at room temperature. (A) LPS-$x$$SiO_2$ ($x$ = 0.02, 0.05, 0.08, 0.1). (B) LPS-$x$$GeO_2$ ($x$ = 0.02, 0.05, 0.08, 0.1). (C) LPS-$x$$SnO_2$ ($x$ = 0.02, 0.05, 0.08, 0.1). Corresponding Arrhenius plots of ionic conductivity of solid electrolytes. (D) LPS-$x$$SiO_2$ ($x$ = 0, 0.02, 0.05, 0.08, 0.1). (E) LPS-$x$$GeO_2$ ($x$ = 0, 0.02, 0.05, 0.08, 0.1). (F) LPS-$x$$SnO_2$ ($x$ = 0, 0.02, 0.05, 0.08, 0.1).

When cations displace $P^{5+}$ ions and bond with $S^{2-}$, two possible scenarios emerge: the replacement of either $P_2S_7^{4-}$ or $PS_4^{3-}$. Importantly, the energy required for substituting $P_2S_7^{4-}$ is lower than that for $PS_4^{3-}$, thus favoring cation doping to favorably target the $P_2S_7^{4-}$[33,34]. Additionally, the ionic radii of $Si^{4+}$, $Ge^{4+}$, and $Sn^{4+}$ are larger than that of $P^{5+}$ ions, which means that cation-doping will broaden the lithium-ion conducting channels and generate lithium defects, thereby facilitating lithium-ion transport.

XPS was employed to assess the effects of doping on the content of $P_2S_7^{4-}$ and $PS_4^{3-}$ structural units. Taking $SnO_2$ doping as an example, Figure 3A shows that in bare LPS, the ratio of $P_2S_7^{4-}$ (131.2 eV) to $PS_4^{3-}$ (132.1 eV) is approximately 1.93:1, closely resembling the theoretical ratio of 2:1[35,36]. With increasing doping levels, a portion of $P_2S_7^{4-}$ is progressively replaced, resulting in diminishing ratios of $P_2S_7^{4-}$ to $PS_4^{3-}$ of 1.87:1, 1.76:1, 1.4:1, and 1.23:1 for LPS-0.02$SnO_2$, LPS-0.05$SnO_2$, LPS-0.08$SnO_2$, and LPS-0.1$SnO_2$, respectively. Assuming that the LPS structure remains unaltered, the theoretical ratios of $P_2S_7^{4-}$ and $PS_4^{3-}$ in LPS-0.08$SnO_2$ and LPS-0.1$SnO_2$ should be 1.84:1 and 1.8:1, respectively. However, the substantial decrease in the proportion of $P_2S_7^{4-}$ groups in LPS doped with 0.08 mol and 0.1 mol $SnO_2$ indicates that the optimal doping amount to maintain the highly conductive LPS phase structure is approximately 0.05 mol. Similarly, the peak intensity of P-S-P in the $P_2S_7^{4-}$ unit [Figure 3B] decreases, while the $Sn^{4+}$ peak in the Sn 3d spectra and $O^{2-}$ peak in the O 1s spectra [Figure 3C and D] increase significantly with increasing the doping contents, indicating an elevated oxide doping level in the electrolytes. Similar trends are also observed in the XPS spectra for samples doped with $SiO_2$ and $GeO_2$ [Supplementary Figures 6 and 7]. Moreover, the XPS peak positions of Si, Ge, and Sn in the doped electrolytes align with the peaks of Si-S, Ge-S, and Sn-S bonds of $Li_{10}SiP_2S_{12}$, $Li_{10}GeP_2S_{12}$, and $Li_{10}SnP_2S_{12}$[37-39], further confirming the successful incorporation of $SiO_2$, $GeO_2$, and $SnO_2$ into the LPS electrolyte.

The oxidative decomposition of solid electrolytes has adverse effects on cathode impedance and overall cell performance. To probe the impact of oxide doping on the oxidative decomposition of LPS-based

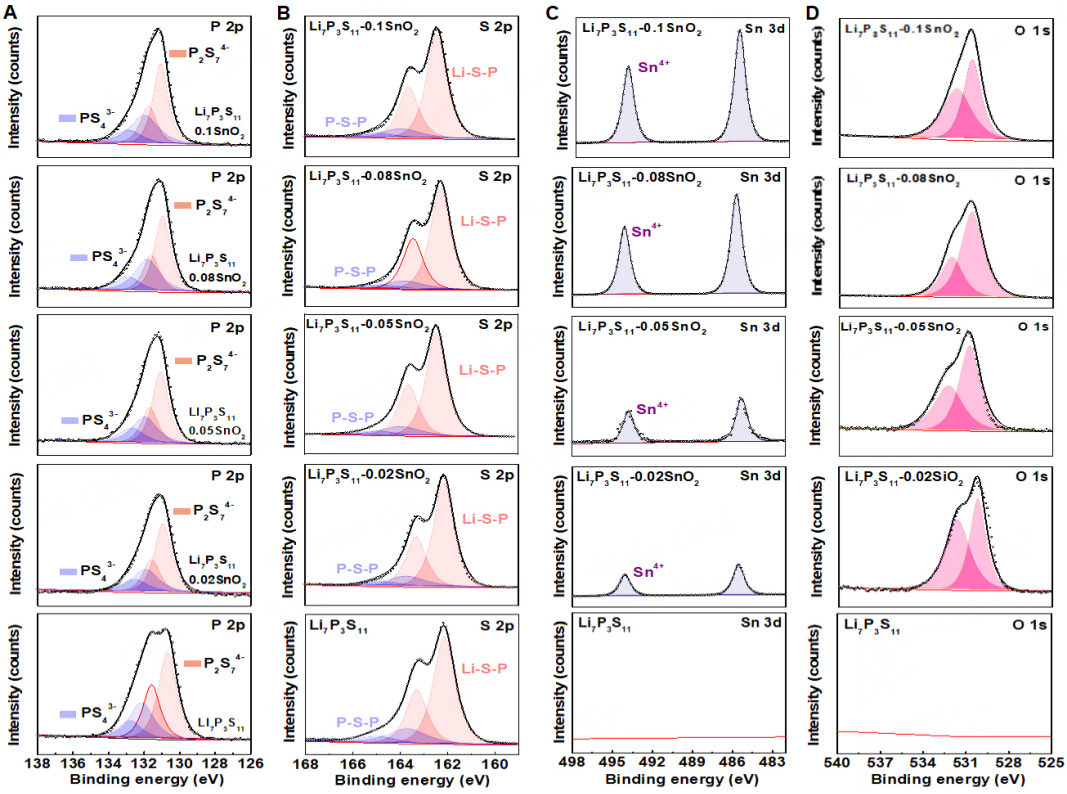


**Figure 3.** XPS spectra of (A) P 2p, (B) S 2p, (C) Sn 3d and (D) O 1s for LPS, LPS-0.02$SnO_2$, LPS-0.05$SnO_2$, LPS-0.08$SnO_2$ and LPS-0.1$SnO_2$.

electrolytes, we employed a half-cell setup, with Li-In serving as the anode and a composite of carbon black (AB) (40 wt.%) mixed with LPS-$x$$MO_2$ (60 wt.%) on the cathode, composite cathode structures greatly increase the contact area and accelerating the kinetic process of electrolyte decomposition, while close contact greatly reduces the interfacial charge transfer resistance and effectively suppresses polarization. Compared to semi-blocking electrodes, mixed electrodes more accurately reflect the conditions in all-solid-state batteries[40]. CV was conducted on the Li-In|LPS-$x$$MO_2$|LPS-$x$$MO_2$-AB cells within a potential range between 2.0 to 4.5 V (*vs.* $Li/Li^+$) at a scan rate of 1 $mVs^{-1}$ [Figure 4]. In the case of the pristine LPS electrolyte, the initial positive sweep from open circuit voltage (OCV) revealed a substantial oxidative peak between 3.0 and 4.5 V, with no discernible reductive peak during the subsequent negative sweep from 4.5 to 2.0 V. During the second cycle, the oxidative peak shifted to a higher voltage, and the intensity of the peak significantly diminished, indicating the passivation of the carbon/LPS-$x$$MO_2$ electrolyte interphase after oxidation. All the doped LPS-$x$$MO_2$ electrolytes exhibited a higher onset oxidative potential, coupled with a lower anodic peak current density during the first cycle compared to the LPS electrolyte. Furthermore, the onset oxidative potential exhibited an increasing trend with rising doping content, concomitant with a noticeable reduction in oxidative peak current density [Supplementary Figure 8]. Similar trends were also observed in the subsequent second cycle. These indicate that the incorporation of $SiO_2$, $GeO_2$, and $SnO_2$ consistently enhanced the oxidative stability of the LPS electrolyte. Among these, LPS-$SiO_2$ demonstrated the lowest oxidative peak current density due to the non-metallic properties of Si[32]. In order to analyze the impact of oxide doping on the interface, EIS and XPS were tested on the (LPS + AB/LPS/Li) cells at different voltages. From Supplementary Figures 9-12, it can be evident that upon charging to 4.5 V, the interfacial impedance experiences a significant increase. Subsequent discharge to 2.0 V results in a decrease in the interfacial impedance. Notably, compared to pristine LPS, the cells with doped electrolytes exhibit a

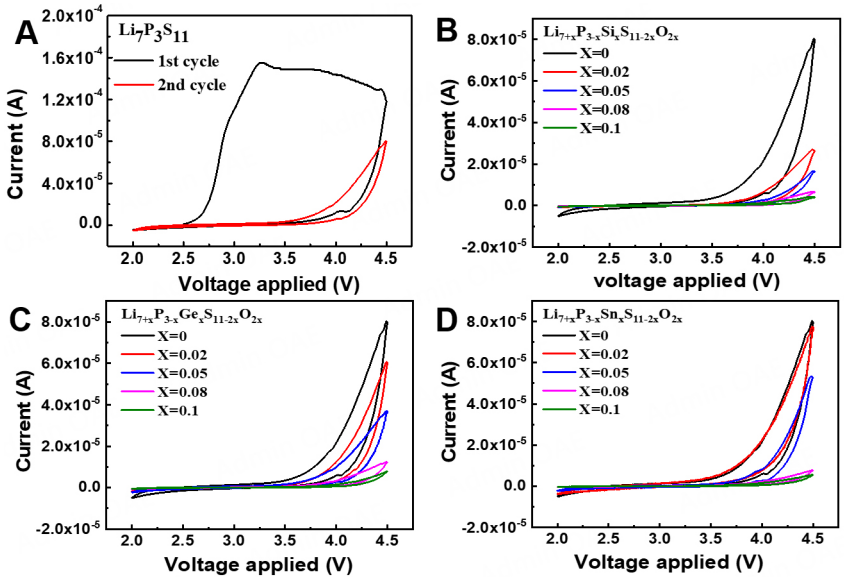


**Figure 4.** CV curves of the Li/SSEs/SSEs + AB cells within the voltage range from 2 to 4.5 V (*vs.* $Li/Li^+$), (A) the first and second cycles curves of LPS, and the second cycle curves of (B) LPS-*x*$SiO_2$ (*x* = 0.02, 0.05, 0.08, 0.1), (C) LPS-*x*$GeO_2$ (*x* = 0.02, 0.05, 0.08, 0.1), (D) LPS-*x*$SnO_2$ (*x* = 0.02, 0.05, 0.08, 0.1)

substantial reduction in interfacial impedance. Moreover, XPS spectra reveal that electrolytes are oxidized at high voltage, forming oxidation products such as elemental sulfur and $P_2S_5$. In the doped electrolyte, sulfate ions are detected. During the subsequent discharge to 2.0 V, the oxidation products decrease. It is worth noting that a small amount of oxidation products is still detected in the XPS spectra of a pristine electrolyte after the charge/discharge process, indicating the irreversible oxidative decomposition of the electrolyte at high voltage. These findings align with the CV results, demonstrating that the incorporation of $SiO_2$, $GeO_2$, and $SnO_2$ can effectively suppress the oxidative decomposition of the LPS-*x*$MO_2$ electrolytes during cycling to high voltage. As illustrated in Supplementary Figure 13 and Supplementary Table 2, the electronic conductivity of the LPS-*x*$MO_2$ electrolytes was assessed through direct current (DC) polarization, employing an ion-blocking cell configuration comprising two blocking electrodes at a bias voltage of 0.5 V. Both the pristine LPS and doped LPS-*x*$MO_2$ electrolytes show a low electronic conductivities of about $1.1\sim1.2 \times 10^{-9}$ S $cm^{-1}$, which are far lower than the ionic conductivities. The similar values of the pristine and doped LPS-*x*$MO_2$ electrolytes suggest that the electronic conductivity does not serve as the decisive factor influencing the electrochemical properties in the doped electrolytes[41-43].

Considering both ionic conductivity and electrochemical stability, LPS-0.05$MO_2$ electrolytes were selected for further electrochemical characterizations. To assess the dendrite-suppressing capability of LPS and LPS-*x*$MO_2$ electrolytes, symmetric Li/LPS-*x*$MO_2$/Li cells were constructed to determine the critical current density[44]. As depicted in Figure 5, the critical current density of the pristine LPS electrolyte is 0.64 mA $cm^{-2}$ at room temperature. In contrast, the doped LPS-*x*$MO_2$ electrolytes exhibit higher critical current densities, with values of 1.14 mA $cm^{-2}$ for LPS-0.05$SiO_2$, 1.02 mA $cm^{-2}$ for LPS-0.05$GeO_2$, and 0.78 mA $cm^{-2}$ for LPS-0.05$SnO_2$, respectively. Notably, LPS-0.05$SiO_2$ displays the highest critical current density, while LPS-0.05$SnO_2$ exhibits a lower polarization voltage. The impact of doping on the stripping/platting behaviors of lithium metal was further assessed using symmetric Li/SSE/Li cells. Supplementary Figure 14 illustrates the time-dependent galvanostatic voltage profiles of the Li/SSE/Li cells operating at 0.1 mA $cm^{-2}$. The Li/LPS/Li cell exhibited the highest overpotential of ~0.03 V. After 40 h of cycling, the voltage curve exhibited a sudden drop, which was attributed to a short circuit induced by the formation of lithium dendrites within

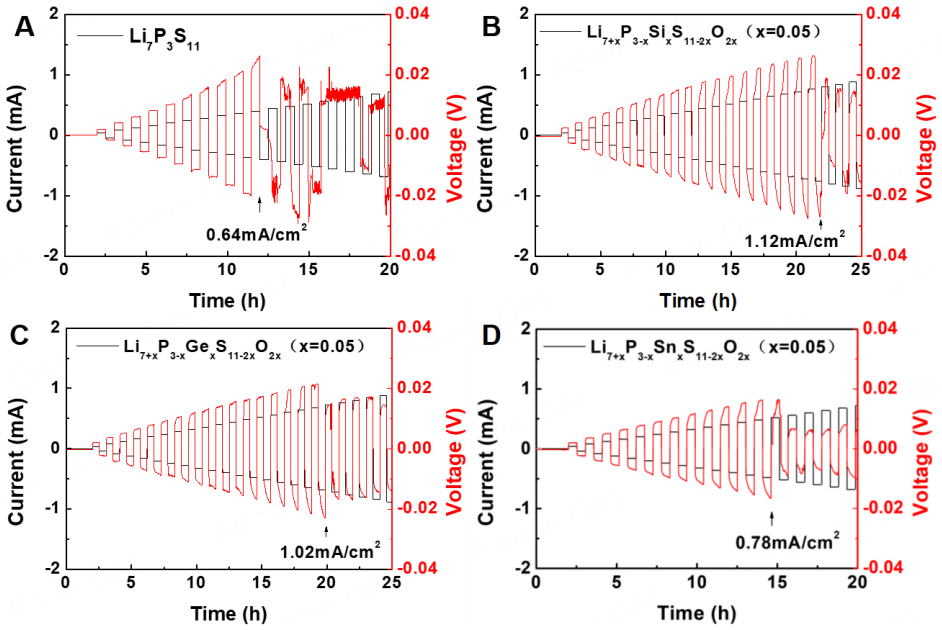


**Figure 5.** Lithium plating/stripping voltage profiles of (A) Li/LPS/Li, (B) Li/LPS-0.05$SiO_2$/Li, (C) Li/LPS-0.05$GeO_2$/Li, and (D) Li/LPS-0.05$SnO_2$/Li cells at different current densities.

the LPS electrolyte. In contrast, the stripping/plating behavior of the symmetric cell utilizing doped LPS-*x*$MO_2$ electrolytes remained stable for 200 h cycling and displayed lower overpotential. This enhanced performance can be attributed to reduced interfacial resistance and improved interfacial stability, thus suppressing lithium dendrite formation. Importantly, among the three doped samples, the SSE doped with $SiO_2$ exhibited the most robust cycling stability, whereas the SSE doped with $SnO_2$ displayed lower polarization voltage.

To investigate the interfacial reactions between the electrolyte and lithium metal, XPS was employed for characterization[45]. The sample doped with $SnO_2$ is used as an example; analysis of XPS spectra [Figure 6] reveals insightful information. In the O 1s spectrum of pristine LPS-0.05$SnO_2$, two distinct peaks are discerned, attributed to P-O-P and Li-O-P interactions. Upon cycling, the O spectrum collected at the Li/LPS-0.05$SnO_2$ interface additionally shows a $Li_2O$ peak at 526.6 eV. The presence of $Li_2O$ in the interphase would modulate interfacial lithium deposition behaviors and maintain the stability of the SSE/Li interphase, thus inhibiting lithium dendrite formation within the SSE[46,47]. The initial S spectrum of LPS-0.05$SnO_2$ is ascribed to non-bridging sulfur Li-S-P and bridging sulfur P-S-P. However, after cycling, the S spectrum at the LPS-0.05$SnO_2$/Li interface exhibits an additional peak at 161.0 eV, attributed to $Li_2S$. Similarly, the P spectrum [Figure 6C] after cycling displays a $Li_3P$ peak (129.3 eV), which was absent in the original sample. As for the pristine LPS electrolyte, the XPS spectra of S 2p and P 2p show similar variations to that of LPS-0.05$SnO_2$. The initial S spectrum is ascribed to non-bridging sulfur Li-S-P and bridging sulfur P-S-P. An additional peak at 161.0 eV, attributed to $Li_2S$, is observed after cycling [Supplementary Figure 15A]. A $Li_3P$ peak (129.3 eV) absent in the original sample can be observed in the P spectrum [Supplementary Figure 15B] after cycling. In pristine LPS-0.05$SnO_2$ electrolyte [Figure 6D], Sn is in the +4 valence state, with binding energies of the Sn 3d5/2 peak at 485.4 eV. After cycling, the collected Sn 3d spectrum at the LPS-0.05$SnO_2$/Li interphase demonstrates an elemental Sn peak at binding energies of 483.7 eV, signifying the reduction of +4 valence Sn at the interphase to elemental Sn by lithium metal[48]. This reduction process results in the formation of a lithium alloy phase at the interphase. A similar

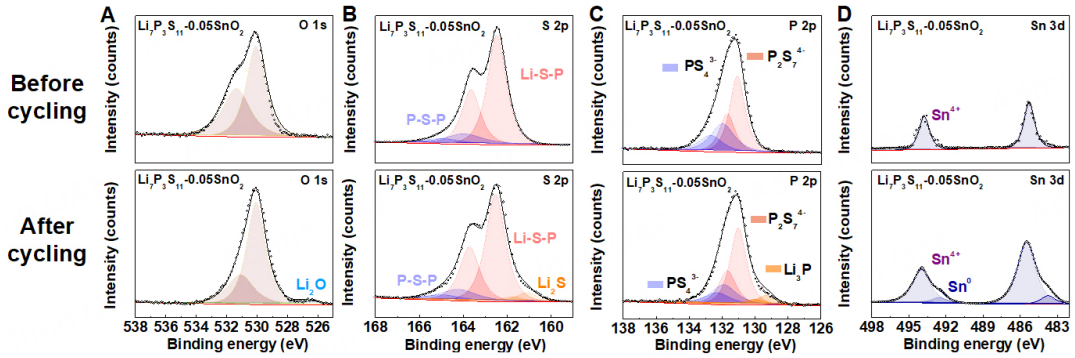


**Figure 6.** XPS spectra of (A) O 1s, (B) S 2p, (C) P 2p, and (D) Sn 3d for LPS-0.05$SnO_2$ sulfide solid electrolytes before and after five cycles.

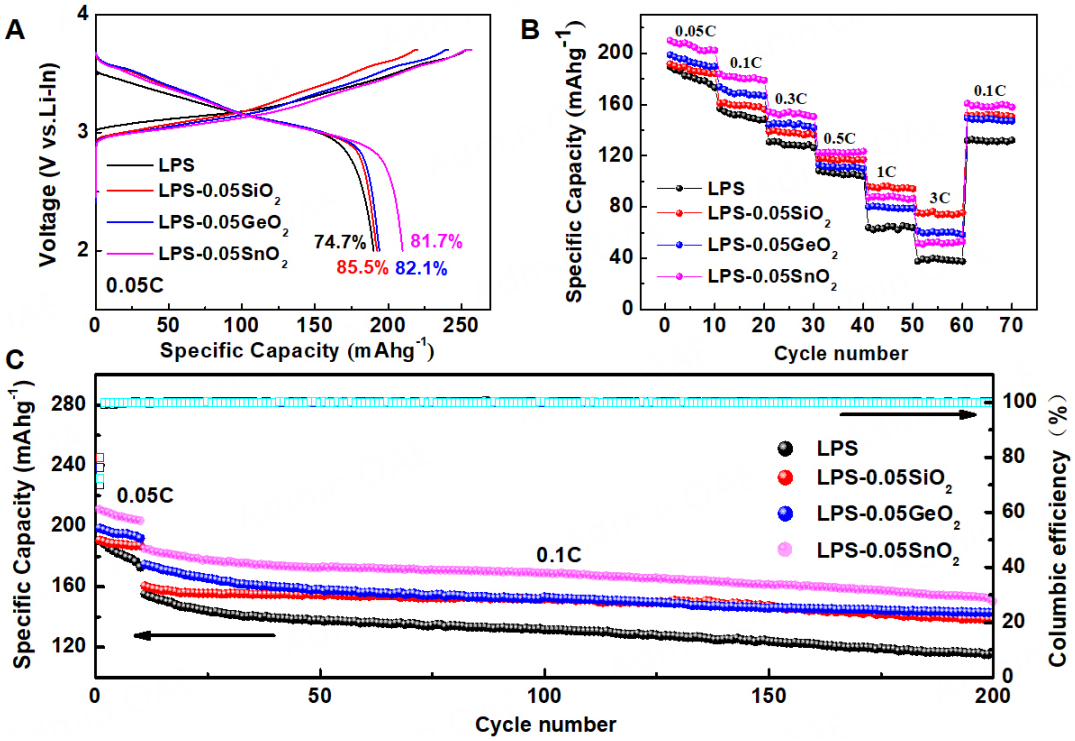


**Figure 7.** Electrochemical performance of the NCM811/SSEs/Li-In ASSLBs, (A) charge-discharge voltage profiles of the first cycle, (B) rate performance at 0.05C, 0.1C, 0.3C, 0.5C, 1C, and 3C, (C) cycling stability, and Coulombic efficiency.

phenomenon is observed in the XPS data of solid electrolytes doped with $SiO_2$ and $GeO_2$ [Supplementary Figure 16]. The formation of $Li_2O$, $Li_2S$, and $Li_3P$ species facilitates the passivation of the Li/electrolyte interphase, which effectively inhibits the continuous reductive degradation of the solid electrolyte.

To further assess the electrochemical performance of the LPS-$x$$MO_2$ electrolyte, ASSLBs were constructed utilizing NCM811 as the cathode material, LPS-$x$$MO_2$ as solid electrolytes, and Li-In as the anode material, respectively. Figure 7A shows the initial charge-discharge voltage profiles of these cells employing various electrolytes. Compared to the bare LPS, the cells with doped LPS-$x$$MO_2$ electrolytes exhibit higher initial coulombic efficiency and improved discharge capacity. This can be attributed to the improved ionic

conductivity and enhanced anodic oxidative stability of the doped LPS-$x$$MO_2$ electrolytes. Notably, among the doped LPS-$x$$MO_2$ electrolytes, the cells with LPS-0.05$SiO_2$ electrolytes show the highest initial coulombic efficiency, whereas the cell with LPS-0.05$SnO_2$ electrolytes demonstrates the highest initial discharge capacity. In addition, Figure 7B illustrates the rate capability of the cells at varying current rates. All the cells employing doped LPS-$x$$MO_2$ electrolytes exhibit improved rate capability compared to the cells with the pristine LPS electrolyte. Although the cells with LPS-0.05$SnO_2$ electrolyte delivers the highest discharge capacity at 0.05 C, the cell with LPS-0.05$SiO_2$ electrolytes shows the best rate capability with a high reversible capacity of 75 mAh/g at 3 C. Furthermore, as depicted in Figure 7C, the cells employing doped LPS-$x$$MO_2$ electrolytes also exhibit enhanced cycling stability compared to the cells with the pristine LPS electrolyte. Following the formation cycles at 0.05C, the bare LPS exhibits an initial discharge capacity of 154.9 mAh·$g^{-1}$ with a capacity retention of 74.63% after 200 cycles at 0.1 C. In comparison, LPS-0.05$SiO_2$ showcases an initial discharge capacity of 160.5 mAh·$g^{-1}$ with a capacity retention of 86%, LPS-0.05$GeO_2$ exhibits an initial discharge capacity of 174.6 mAh·$g^{-1}$ with a capacity retention of 81.8%, and LPS-0.05$SnO_2$ displays an initial discharge capacity of 184.9 mAh·$g^{-1}$ with a capacity retention of 81.1%. These results indicate that while the cell with LPS-0.05$SnO_2$ electrolyte demonstrates higher initial capacity, LPS-0.05$SiO_2$ electrolytes offer superior initial coulombic efficiency, rate capability, and cycling stability. This observation aligns with the previously conducted assessments of ionic conductivity and oxidative stability, wherein the LPS-0.05$SiO_2$ electrolyte demonstrated the highest oxidative stability, while the LPS-0.05$SnO_2$ electrolyte exhibited the highest ionic conductivity.

## CONCLUSIONS

In summary, an anion and cation co-doping strategy is proposed to functionally enhance both the ionic conductivity and electrochemical stability of the LPS-based sulfide electrolyte. A series of $SiO_2$-, $GeO_2$-, and $SnO_2$-doped $Li_{7+x}P_{3-x}M_xS_{11-2x}O_{2x}$ (M = Si, Ge, Sn, $x$ = 0, 0.02, 0.05, 0.08, 0.1) sulfide solid electrolytes are prepared via high-energy ball milling and sintering. The effects of doping on the structural and electrochemical properties were systematically screened. XPS characterization indicates that the cations demonstrate a preference for substituting the $P^{5+}$ of the $P_2S_7^{4-}$ unit within the LPS matrix, which expands the $Li^+$ transport channels and generates lithium defects to facilitate ion conduction. This significantly enhances the ionic conductivity of the doped LPS-$x$$MO_2$ electrolytes. The LPS-0.05$SnO_2$ electrolyte exhibits a high ionic conductivity of 2.53 × $10^{-3}$ S $cm^{-1}$, which is 2.5 times higher than the pristine LPS electrolyte. Further improving the doping levels hinders lithium-ion migration, resulting in elevated activation energy and decreased ionic conductivity. The oxide doping also significantly improves the oxidative stability of the LPS-$x$$MO_2$ electrolytes, which is crucial for maintaining stable electrode/electrolyte interphases. While the LPS-0.05$SnO_2$ electrolyte delivers higher ionic conductivity, the LPS-0.05$SiO_2$ electrolyte demonstrates superior oxidative stability and higher critical current density. The NCM811-based ASSLBs utilizing the doped LPS-0.05$MO_2$ electrolytes exhibit higher coulombic efficiency, superior discharge capacity, rate capability, and cycling stability compared to the pristine LPS electrolyte. The cell utilizing the LPS-0.05$SnO_2$ electrolyte exhibits a higher initial capacity, whereas the LPS-0.05$SiO_2$ electrolyte demonstrates superior initial coulombic efficiency, rate capability, and cycling stability. This is consistent with the characterization results of ionic conductivity and electrochemical stability, where the LPS-0.05$SiO_2$ electrolyte shows higher oxidative stability and the LPS-0.05$SnO_2$ electrolyte exhibits superior ionic conductivity. These findings shed light on doping strategies for optimizing solid electrolyte materials toward the development of high-performance ASSLBs.

## DECLARATIONS

### Authors' contributions

Methodology, formal analysis, and writing of the manuscript: Li C, Lv Z,

Data analysis and technical support: Wu Y, Peng J
Data acquisition: Liu J, Zheng X
Analysis and interpretation of the results: Wu Y, Tang W
Supervision, writing - review and editing: Gong Z, Yang Y
All authors discussed the results and commented on the manuscript.

### Availability of data and materials

The data supporting our findings can be found in the Supplementary Material.

### Financial support and sponsorship

This work was supported by the National Natural Science Foundation of China (grants no. 22279108, 22261160570, 21935009, and 22021001) and the National Key R&D Program of China (grant no. 2021YFB2401800).

### Conflicts of interest

All authors declared that there are no conflicts of interest.

### Ethical approval and consent to participate

Not applicable.

### Consent for publication

Not applicable.



## REFERENCES

1. Liu J, Zhang YH, Zhou JQ, et al. Advances and prospects in improving the utilization efficiency of lithium for high energy density lithium batteries. *Adv Funct Mater* 2023;33:2302055. DOI
2. Sandstrom SK, Ji X. Reversible halogen cathodes for high energy lithium batteries. *Joule* 2023;7:13-4. DOI
3. Sang J, Tang B, Pan K, He YB, Zhou Z. Current status and enhancement strategies for all-solid-state lithium batteries. *Acc Mater Res* 2023;4:472-83. DOI
4. An W, Gao B, Mei SX, et al. Scalable synthesis of ant-nest-like bulk porous silicon for high-performance lithium-ion battery anodes. *Nat Commun* 2019;10:1447. DOI PubMed PMC
5. Zhang QB, Chen HX, Luo LL, et al. Harnessing the concurrent reaction dynamics in active Si and Ge to achieve high performance lithium-ion batteries. *Energy Environ Sci* 2018;11:669-81. DOI
6. Ma QY, Zheng Y, Luo D, et al. 2D materials for all-solid-state lithium batteries. *Adv Mater* 2022;34:e2108079. DOI
7. Sun CW, Liu J, Gong YD, Wilkinson DP, Zhang JJ. Recent advances in all-solid-state rechargeable lithium batteries. *Nano Energy* 2017;33:363-86. DOI
8. Xiao YH, Wang Y, Bo SH, Kim JC, Miara LJ, Ceder G. Understanding interface stability in solid-state batteries. *Nat Rev Mater* 2020;5:105-26. DOI
9. Zhao Q, Stalin S, Zhao CZ, Archer LA. Designing solid-state electrolytes for safe, energy-dense batteries. *Nat Rev Mater* 2020;5:229-52. DOI
10. Xu J, Liu L, Yao N, Wu F, Li H, Chen LQ. Liquid-involved synthesis and processing of sulfide-based solid electrolytes, electrodes, and all-solid-state batteries. *Mater Today Nano* 2019;8:100048. DOI
11. Lau J, Deblock RH, Butts DM, Ashby DS, Choi CS, Dunn BS. Sulfide solid electrolytes for lithium battery applications. *Adv Energy Mater* 2018;8:1800933. DOI
12. Wu JH, Liu SF, Han FD, Yao XY, Wang CS. Lithium/sulfide all-solid-state batteries using sulfide electrolytes. *Adv Mater* 2021;33:e2000751. DOI
13. Wang S, Fang RY, Li YT, et al. Interfacial challenges for all-solid-state batteries based on sulfide solid electrolytes. *J Materiomics* 2021;7:209-18. DOI
14. Culver SP, Koerver R, Zeier WG, Janek J. On the functionality of coatings for cathode active materials in thiophosphate-based all-solid-state batteries. *Adv Energy Mater* 2019;9:1900626. DOI

15. Lian PJ, Zhao BS, Zhang LQ, Xu N, Wu MT, Gao XF. Inorganic sulfide solid electrolytes for all-solid-state lithium secondary batteries. *J Mater Chem A* 2019;7:20540-57. DOI
16. Zhu YZ, Mo YF. Materials design principles for air-stable lithium/sodium solid electrolytes. *Angew Chem Int Ed* 2020;59:17472-6. DOI PubMed
17. Ohtomo T, Hayashi A, Tatsumisago M, Kawamoto K. All-solid-state batteries with $Li_2O$-$Li_2S$-$P_2S_5$ glass electrolytes synthesized by two-step mechanical milling. *J Solid State Electrochem* 2013;17:2551-7. DOI
18. Zhao FP, Liang JW, Yu C, et al. A versatile Sn-substituted argyrodite sulfide electrolyte for all-solid-state Li metal batteries. *Adv Energy Mater* 2020;10:1903422. DOI
19. Wang YQ, Lü XJ, Zheng C, et al. Chemistry design towards a stable sulfide-based superionic conductor $Li_4Cu_8Ge_3S_{12}$. *Angew Chem Int Ed* 2019;58:7673-7. DOI PubMed PMC
20. Zhang ZR, Zhang JX, Sun YL, et al. $Li_{4-x}SbSn_{1-x}S_4$ solid solutions for air-stable solid electrolytes. *J Energy Chem* 2020;41:171-6. DOI
21. Tufail MK, Zhou L, Ahmad N, et al. A novel air-stable $Li_7Sb_{0.05}P_{2.95}S_{10.5}I_{0.5}$ superionic conductor glass-ceramics electrolyte for all-solid-state lithium-sulfur batteries. *Chem Eng J* 2021;407:127149. DOI
22. Zhao BS, Wang L, Chen P, et al. Congener substitution reinforced $Li_7P_{2.9}Sb_{0.1}S_{10.75}O_{0.25}$ glass-ceramic electrolytes for all-solid-state lithium-sulfur batteries. *ACS Appl Mater Interfaces* 2021;13:34477-85. DOI
23. Ni Y, Huang C, Liu H, Liang YH, Fan LZ. A high air-stability and Li-metal-compatible $Li_{3+2x}P_{1-x}Bi_xS_{4-1.5x}O_{1.5x}$ sulfide electrolyte for all-solid-state Li-metal batteries. *Adv Funct Mater* 2022;32:2205998. DOI
24. Rajagopal R, Subramanian Y, Jung YJ, Kang S, Ryu KS. Preparation of metal-oxide-doped $Li_7P_2S_8Br_{0.25}I_{0.75}$ solid electrolytes for all-solid-state lithium batteries. *ACS Appl Mater Interfaces* 2023;15:21016-26. DOI PubMed
25. Zhang N, Wang L, Diao QY, et al. Mechanistic insight into $La_2O_3$ dopants with high chemical stability on $Li_3PS_4$ sulfide electrolyte for lithium metal batteries. *J Electrochem Soc* 2022;169:020544. DOI
26. Liu GZ, Xie DJ, Wang XL, et al. High air-stability and superior lithium ion conduction of $Li_{3+3x}P_{1-x}Zn_xS_{4-x}O_x$ by aliovalent substitution of ZnO for all-solid-state lithium batteries. *Energy Stor Mater* 2019;17:266-74. DOI
27. Ahmad N, Zhou L, Faheem M, et al. Enhanced air stability and high Li-ion conductivity of $Li_{6.988}P_{2.994}Nb_{0.2}S_{10.934}O_{0.6}$ glass-ceramic electrolyte for all-solid-state lithium-sulfur batteries. *ACS Appl Mater Interfaces* 2020;12:21548-58. DOI
28. Xu RC, Xia XH, Li SH, Zhang SZ, Wang XL, Tu JP. All-solid-state lithium-sulfur batteries based on a newly designed $Li_7P_{2.9}Mn_{0.1}S_{10.7}I_{0.3}$ superionic conductor. *J Mater Chem A* 2017;5:6310-7. DOI
29. Wang ZX, Jiang Y, Wu J, et al. Reaction mechanism of $Li_2S$-$P_2S_5$ system in acetonitrile based on wet chemical synthesis of $Li_7P_3S_{11}$ solid electrolyte. *Chem Eng J* 2020;393:124706. DOI
30. Dietrich C, Weber DA, Sedlmaier SJ, et al. Lithium ion conductivity in $Li_2S$-$P_2S_5$ glasses - building units and local structure evolution during the crystallization of superionic conductors $Li_3PS_4$, $Li_7P_3S_{11}$ and $Li_4P_2S_7$. *J Mater Chem A* 2017;5:18111-9. DOI
31. Wang CH, Adair KR, Liang JW, et al. Solid-state plastic crystal electrolytes: effective protection interlayers for sulfide-based all-solid-state lithium metal batteries. *Adv Funct Mater* 2019;29:1900392. DOI
32. Wang ZX, Jiang Y, Wu J, et al. Doping effects of metal cation on sulfide solid electrolyte/lithium metal interface. *Nano Energy* 2021;84:105906. DOI
33. Kamaya N, Homma K, Yamakawa Y, et al. A lithium superionic conductor. *Nat Mater* 2011;10:682-6. DOI
34. Liu H, Zhu QS, Liang YH, et al. Versatility of Sb-doping enabling argyrodite electrolyte with superior moisture stability and Li metal compatibility towards practical all-solid-state Li metal batteries. *Chem Eng J* 2023;462:142183. DOI
35. Busche MR, Weber DA, Schneider Y, et al. *In situ* monitoring of fast Li-ion conductor $Li_7P_3S_{11}$ crystallization inside a hot-press setup. *Chem Mater* 2016;28:6152-65. DOI
36. Rangasamy E, Sahu G, Keum JK, Rondinone AJ, Dudney NJ, Liang C. A high conductivity oxide-sulfide composite lithium superionic conductor. *J Mater Chem A* 2014;2:4111-6. DOI
37. Mishra GK, Gautam M, Bhawana K, Chakrabarty N, Mitra S. Germanium-free dense lithium superionic conductor and interface re-engineering for all-solid-state lithium batteries against high-voltage cathode. *ACS Appl Mater Interfaces* 2023;15:10629-41. DOI PubMed
38. Wenzel S, Randau S, Leichtweiß T, et al. Direct observation of the interfacial instability of the fast ionic conductor $Li_{10}GeP_2S_{12}$ at the lithium metal anode. *Chem Mater* 2016;28:2400-7. DOI
39. Zheng BZ, Liu XS, Zhu JP, et al. Unraveling (electro)-chemical stability and interfacial reactions of $Li_{10}SnP_2S_{12}$ in all-solid-state Li batteries. *Nano Energy* 2020;67:104252. DOI
40. Han FD, Zhu YZ, He XF, Mo YF, Wang CS. Electrochemical stability of $Li_{10}GeP_2S_{12}$ and $Li_7La_3Zr_2O_{12}$ solid electrolytes. *Adv Energy Mater* 2016;6:1501590. DOI
41. Han FD, Westover AS, Yue J, et al. High electronic conductivity as the origin of lithium dendrite formation within solid electrolytes. *Nat Energy* 2019;4:187-96. DOI
42. Mo FJ, Ruan JF, Sun SX, et al. Inside or outside: origin of lithium dendrite formation of all solid-state electrolytes. *Adv Energy Mater* 2019;9:1902123. DOI
43. Raj R, Wolfenstine J. Current limit diagrams for dendrite formation in solid-state electrolytes for Li-ion batteries. *J Power Sources* 2017;343:119-26. DOI
44. Jiang Y, Wang ZX, Xu CX, et al. Atomic layer deposition for improved lithiophilicity and solid electrolyte interface stability during lithium plating. *Energy Stor Mater* 2020;28:17-26. DOI

45. Su YB, Ye LH, Fitzhugh W, et al. A more stable lithium anode by mechanical constriction for solid state batteries. *Energy Environ Sci* 2020;13:908-16. DOI
46. He XZ, Ji X, Zhang B, et al. Tuning interface lithiophobicity for lithium metal solid-state batteries. *ACS Energy Lett* 2022;7:131-9. DOI
47. Hou WH, Zhou P, Gu HH, et al. Fluorinated carbamate-based electrolyte enables anion-dominated solid electrolyte interphase for highly reversible Li metal anode. *ACS Nano* 2023;17:17527-35. DOI
48. Huang YL, Shao BW, Han FD. Li alloy anodes for high-rate and high-areal-capacity solid-state batteries. *J Mater Chem A* 2022;10:12350-8. DOI